Vortex Pattern Stabilization in Thin Films Resulting from Shear Thickening of Active Suspensions

Henning Reinken[*] and Andreas M. Menzel[†]

Institut für Physik, Otto-von-Guericke-Universität Magdeburg, Universitätsplatz 2, 39106 Magdeburg, Germany

The need for structuring on micrometer scales is abundant, for example, in view of phononic applications. We here outline a novel approach based on the phenomenon of active turbulence on the mesoscale. As we demonstrate, a shear-thickening carrier fluid of active microswimmers intrinsically stabilizes regular vortex patterns of otherwise turbulent active suspensions. The fluid self-organizes into a periodically structured nonequilibrium state. Introducing additional passive particles of intermediate size leads to regular spatial organization of these objects. Our approach opens a new path toward functionalization through patterning of thin films and membranes.

Structuring materials on micrometer and submicrometer scales is of central importance to various types of prospective applications of functionalized components, such as shape-changing nematic elastomers [1–4] or phononic metamaterials [5]. The latter provide, for instance, acoustic band gaps [6–8]. This function relies on spatially organizing colloidal particles on scales responsive to acoustic excitations. Generally, such structuring requires measures imposed from outside. We here introduce a strategy that facilitates intrinsic patterning through nonequilibrium effects. It relies on self-supported regular organization of vortices in an otherwise turbulent suspension of active microswimmers. Key to this mechanism is a shear-thickening carrier fluid.

Suspensions of microswimmers are a subclass of active matter [9–13]. The interplay with the surrounding fluid determines both the swimming behavior of individual swimmers and their mutual interactions. These nonequilibrium systems are amenable to structure formation. For example, bacterial suspensions develop turbulent states, swirling, and vortex formation [14–19] despite prevailing low-Reynolds-number conditions. Being able to control or switch between different patterns is important for possible applications such as microscale extraction of work [20,21], microfluidic mixing [22,23], or cargo transport [24–26]. In particular, regular mesoscale patterning is eminent when creating functionalized materials. Previous experimental and theoretical studies have shown that external fields [27] or geometrical constraints such as coupled flow chambers [28–30] or small obstacles [31–34] can stabilize regular vortex patterns [31,33,35]. However, it is desirable to achieve such regular structure formation intrinsically, without the need of external intervention.

Many previous considerations on microswimmers and their collective behavior assume the solvent to be Newtonian, although many biological fluids actually exhibit non-Newtonian rheology or viscoelasticity. Few recent exceptions deal with the effects of viscoelasticity [36–41]. Non-Newtonian behavior, such as shear thickening and shear thinning, have been addressed [42–47], but only a limited number of studies explore resulting collective dynamics [48–55]. The impact of the non-Newtonian effect of shear thickening on the complex pattern formation in active fluids has not been explored so far.

Here, we turn to this open question, based on previous descriptions of the dynamics in suspensions of active microswimmers [56–59]. Past investigations correctly predicted the main features of mesoscale turbulence [60], a dynamic state of vortex formation on an intermediate length scale much larger than the single-swimmer scale [17,60]. We now incorporate non-Newtonian effects by a viscosity that increases with local shear rate. Our results show that such shear thickening stabilizes regular structures, specifically centered rectangular latticelike patterns consisting of elongated vortices. Remarkably, geometrical constraints or other externally applied means of control are not necessary for this dynamic rotational symmetry breaking associated with anisotropic regular pattern formation. Moreover, introducing passive particles larger than the active swimmers leads to their spatial organization and regular patterning according to the vortex patterns. In this way, we reveal a novel path toward structuring and functionalization of thin metamaterials.

We describe the dynamics of the active suspension by a generalized, incompressible Navier-Stokes equation for the overall velocity field $\mathbf{v}(\mathbf{x}, t)$ of the entire suspension,

$$\partial_t \mathbf{v} + \mathbf{v} \cdot \nabla \mathbf{v} = -\nabla \tilde{p} + \nabla \cdot \tilde{\boldsymbol{\sigma}}, \qquad \nabla \cdot \mathbf{v} = 0, \quad (1)$$

rendering the approach Galilei invariant. Here, the constant density ρ is absorbed into the pressure p ($\tilde{p} = p/\rho$) and the

stress tensor $\boldsymbol{\sigma}$ ($\tilde{\boldsymbol{\sigma}} = \boldsymbol{\sigma}/\rho$). Following recent achievements to include the energy input by the microswimmers [56–58], we expand the stress tensor in gradients of the deformation rate $\boldsymbol{\Sigma} = [(\nabla\mathbf{v}) + (\nabla\mathbf{v})^\top]/2$,

$$\tilde{\boldsymbol{\sigma}} = (\Gamma_0 + \Gamma_2\nabla^2 + \Gamma_4\nabla^4)[(\nabla\mathbf{v}) + (\nabla\mathbf{v})^\top], \quad (2)$$

where $\top$ marks the transpose. Often, the active stress includes orientational order parameter fields, which are governed by additional dynamic equations [11,18]. In our case, the orientational order parameters are "slaved" to the suspension velocity [58]. In principle, one can include terms $\propto \mathbf{vv} - |\mathbf{v}|^2\mathbf{I}/d$, where $\mathbf{I}$ is the unit tensor and d spatial dimensionality. However, these terms would only lead to a rescaling of the nonlinear advection term and an additional contribution to the pressure [56]. Equation (2) captures essential experimental observations on active suspensions, for example, length scale selection and emergence of turbulent vortex patterns [56]. Very good agreement with both bacterial microswimmers and adenosine triphosphate-driven microtubular networks has been demonstrated [58]. Recent work on *passive* suspensions showed that higher-order gradients of the suspension-averaged velocity can emerge in the effective stress tensor within a rigorous derivation [61], which further supports our approach.

Positive values of the coefficients Γ_0 and Γ_4 ensure asymptotic stability at long and short wavelengths, respectively [56]. In the passive case, $\Gamma_4 = 0$, $\Gamma_2 = 0$, and $\Gamma_0 = \nu$, introducing the kinematic viscosity ν. In the active case, we adopt $\Gamma_0 = \nu$, while Γ_2 can show either sign. For $\Gamma_2 < 0$, there is no active energy input and the quiescent state $\mathbf{v}(\mathbf{x}, t) = \mathbf{0}$ is stable. Instead, for $\Gamma_2 > 0$, active stresses set in, which can excite intermediate wavelengths [56]. Thus, Γ_2 characterizes the strength of activity. When increasing $\Gamma_2 > \sqrt{4\nu\Gamma_4}$, linear stability analysis yields a finite-wavelength instability of critical wave number $k_c = \sqrt{\Gamma_2/(2\Gamma_4)}$. Further increasing Γ_2, a band of unstable modes emerges, indicating wave numbers at which activity pumps energy into the system. Similarly to driven Navier-Stokes fluids [62], the nonlinear advection term $\mathbf{v} \cdot \nabla\mathbf{v}$ relates to turbulence and energy transport between wave numbers. However, driving in our case is internal, due to the active energy input by the microswimmers. Resulting balances of active energy input and dissipation lead to statistically stationary states, in line with main features of experimental observations on bacterial suspensions [56]. Recent studies employing a similar description suggest a transition between different spectral scaling regimes in active turbulence upon an increase of activity [63]. In this context, we here focus on the *mildly* active regime, see Ref. [63], where the statistics of velocity increments follows a Gaussian distribution.

Shear thickening of the carrier liquid is described by a viscosity increasing with local shear rates $\dot{\gamma}(\mathbf{x})$. We consider a so-called power-law fluid [64–66] of constant zero-shear viscosity ν_0,

$$\nu(\mathbf{x}) = \nu_0 + \nu_0 \left(\frac{\dot{\gamma}(\mathbf{x})}{\dot{\gamma}_2}\right)^{n-1}, \quad (3)$$

where $\dot{\gamma}(\mathbf{x}) = \sqrt{2\boldsymbol{\Sigma}(\mathbf{x}):\boldsymbol{\Sigma}(\mathbf{x})}$. The exponent n determines how the viscosity $\nu(\mathbf{x})$ increases with local shear rate $\dot{\gamma}(\mathbf{x})$. $\dot{\gamma}_2$ is a reference shear rate, indicating when the viscosity reaches $2\nu_0$.

We now rescale lengths by k_c^{-1}, times by $(k_c^2\nu_0)^{-1}$, and thus velocities by $k_c\nu_0$. As a result, Eq. (1) becomes

$$\partial_t\mathbf{v} + \mathbf{v} \cdot \nabla\mathbf{v} = -\nabla\tilde{p} + \nabla \cdot (2\nu\boldsymbol{\Sigma}) + a(2\nabla^4\mathbf{v} + \nabla^6\mathbf{v}), \quad (4)$$

where $\nu = 1 + (\sqrt{2\boldsymbol{\Sigma}:\boldsymbol{\Sigma}}/\dot{\gamma}_2)^{n-1}$. In our incompressible system, $\tilde{p}$ merely acts as a Langrange multiplier ensuring $\nabla \cdot \mathbf{v} = 0$. The parameter $a = \Gamma_2^2/(4\nu_0\Gamma_4)$ sets the strength of active energy input relative to the zero-shear viscosity ν_0. For $a < 1$, the isotropic, quiescent state $\mathbf{v}(\mathbf{x}, t) = \mathbf{0}$ is stable, implying that the active energy input does not suffice to overcome viscous dissipation. Thus, pattern formation is not observed. Conversely, for $a > 1$, the system forms flow patterns characterized by a specific length scale set by the fastest-growing mode k_m. Close to the transition, $k_m = k_c = 1$, yielding a length scale of $\Lambda_c = 2\pi/k_c$. For $a = 0$, we recover the passive Navier-Stokes equation for non-Newtonian, shear-thickening behavior.

We employ a pseudo-spectral method to solve Eq. (4) in a two-dimensional system with periodic boundary conditions starting from random initial values; for details, see the Supplemental Material [67], which includes Refs. [68–73]. The system size is set to $48\pi \times 48\pi$, much larger than the critical length scale $\Lambda_c = 2\pi$. Varying the values of activity a, power-law exponent n, and reference shear rate $\dot{\gamma}_2$, we investigate the emerging patterns. Examples are illustrated in Fig. 1, where snapshots of the vorticity field $\omega = (\nabla \times \mathbf{v})_z$ are shown for $a = 1.1$, $n = 3$, and varying $\dot{\gamma}_2$.

For high reference shear rate $\dot{\gamma}_2$, that is, closer to Newtonian behavior, the system develops a turbulent state, similar to the case without shear thickening [56–58]; see Fig. 1(c). However, when $\dot{\gamma}_2$ is low, a rather regular state emerges, which can be characterized as a centered rectangular lattice of vortices. Figure 1(a) shows the vorticity field in this state. The vortices become elongated along a common axis, displaying an aspect ratio of about 3. For intermediate values of $\dot{\gamma}_2$, the system develops a state of still clearly visible anisotropy of the vortices, see Fig. 1(b), yet not stationary. Instead, numerous defects and dynamic reorganization occur.

To further characterize the observed spatiotemporal patterns, we first calculate the correlation time τ [67], which quantifies how quickly the velocity field reorganizes. Figure 2(a) shows τ in a-$\dot{\gamma}_2$ space for different values of n. Consistent with our previous observations, we find that τ is small for large values of both a and $\dot{\gamma}_2$, indicating a
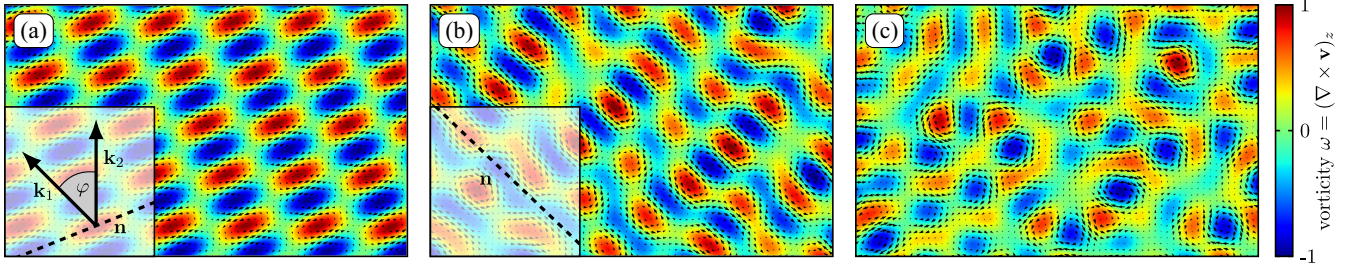
FIG. 1. Snapshots of the vorticity field $\omega(\mathbf{x}, t)$ at $a = 1.1$ and $n = 3$ at arbitrarily chosen times t for different values of the reference shear rate: (a) $\dot{\gamma}_2 = 0.1$, (b) $\dot{\gamma}_2 = 0.9$, and (c) $\dot{\gamma}_2 = 2.5$. Arrows denote the velocity field $\mathbf{v}$. Both quantities are rescaled for visualization purposes. (a) For very small $\dot{\gamma}_2$, the flow field settles into a stationary vortex lattice, where vortices are elongated along the director $\mathbf{n}$ shown as the dashed line in the inset. The structure can be represented by two wave vectors forming an angle $\varphi = \pi/4$ (inset). For larger $\dot{\gamma}_2$, the flow field becomes increasingly irregular. In (b), the vortices are still visibly aligned along a common director $\mathbf{n}$ (inset), whereas the rotational order is lost in (c). The size of the snapshots is $16\pi \times 10\pi$.

turbulent state. Decreasing either a or $\dot{\gamma}_2$ increases τ, and the dynamics becomes slower until the emerging patterns settle into a stationary state for very small values of a and $\dot{\gamma}_2$. Since the system does not rearrange anymore, τ diverges. Besides, τ tends to decrease for increasing n, so that smaller n stabilize the regular elongated vortex structure. For comparison, τ as a function of a is shown on the right-hand side of Fig. 2(a) for a Newtonian suspension without shear thickening ($\nu = 1$). In this case, larger values of a lead to an increased input of active energy into the system and, thus, to a more turbulent state.

In Figs. 1(a) and 1(b), the elongated vortices on average align along a common axis. Thus, we determine the global nematic order parameter q for orientational order of elongated vortices [67]. $|q| = 0$ for a flow field of uniformly distributed vortex orientations, whereas $|q| = 1$ for completely ordered systems, such as in Fig. 1(a). Figure 2(b) shows $|q|$ for different values of n. For smaller reference

shear rate $\dot{\gamma}_2$, we indeed find that the elongated vortices are aligned along a common axis $\mathbf{n}$; see Figs. 1(a) and 1(b). Thus, shear thickening does not only lead to local vortex elongation, but also to spontaneous overall rotational symmetry breaking. The system exhibits global nematic order even for values of $\dot{\gamma}_2$ associated with defects and reorganization as in Fig. 1(b). For developed turbulence, $|q|$ approaches zero; see the right-hand side of Fig. 2(b). Again, we find that increasing n reduces stabilization of the elongated vortex pattern and thus suppresses $|q|$. Moreover, the impact of activity a on stabilization seems to diminish.

Conceptually, the shear-thickening properties of the suspension provide a saturation mechanism for the growing vortex patterns that does not rely on the turbulent energy transfer to larger scales and subsequent dissipation. As a result, regular structures are stabilized. To shed more light on these effects, we determine associated amplitude
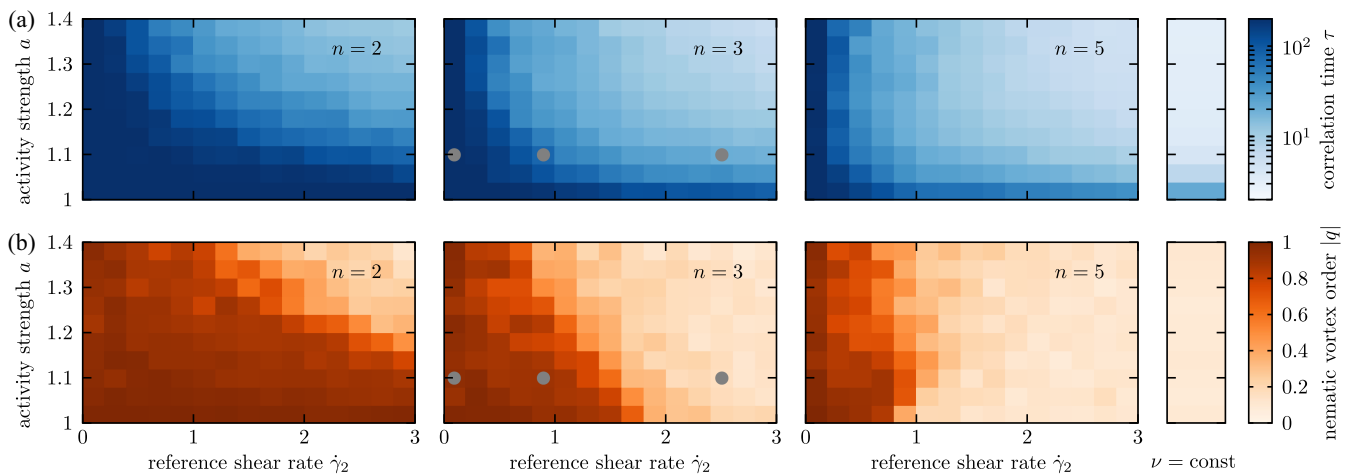

FIG. 2. Characteristic quantities as a function of a and $\dot{\gamma}_2$ for different values of n. (a) Correlation time τ on a log scale. (b) Nematic order parameter $|q|$ for the elongated vortices. High nematic order for small values of $\dot{\gamma}_2$ signifies a globally ordered vortex structure with broken rotational symmetry. The gray circles in the plots for $n = 3$ indicate the parameter values where the snapshots shown in Fig. 1 are taken. The column on the right-hand side includes the Newtonian case ($\nu = 1$) for comparison.

equations. The stationary, centered rectangular lattice close to its emergence forms an orthorhombic state that is represented by two modes of complex amplitudes A_1 and A_2 and wave vectors $\mathbf{k}_1$ and $\mathbf{k}_2$ [74]. As inferred from the linear stability analysis outlined above, the isotropic state becomes unstable to the growth of perturbations of wave vectors $|\mathbf{k}| = k_c = 1$ when activity is increased above $a = 1$. Close to this critical point, we assume the length scale $\Lambda_c = 2\pi/k_c$ to dominate the emerging patterns. We write the wave vectors of the modes $\mathbf{k}_i$ ($i = 1,\ 2$) as $\mathbf{k}_i = k_c(\cos\varphi_i, \sin\varphi_i)$. Without loss of generality, we set one of the angles to zero, $\varphi_1 = 0$. Then $\varphi_2 = \varphi$ determines the relative angle between the wave vectors. Thus, vortex structures as in Fig. 1(a) are parametrized by

$$v_x = A_2 \sin(\varphi)e^{i[\cos(\varphi)x+\sin(\varphi)y]} + \text{c.c.},$$
$$v_y = -A_1 e^{ix} - A_2 \cos(\varphi)e^{i[\cos(\varphi)x+\sin(\varphi)y]} + \text{c.c.}, \quad (5)$$

satisfying incompressibility, where c.c. denotes complex conjugates.

Inserting Eq. (5) into Eq. (4), we restrict ourselves to values $n = 3$ and 5 to make analytical progress; see also Ref. [67]. Using symbolic computation software [75] and collecting terms $\sim e^{ix}$ and $\sim e^{i[\cos(\varphi)x+\sin(\varphi)y]}$, we find for $n = 3$ [67]

$$\frac{\partial A_1}{\partial t} = (a-1)A_1 - \frac{A_1}{\dot{\gamma}_2^2}\{3|A_1|^2 + 2|A_2|^2[2+\cos(4\varphi)]\},$$
$$\frac{\partial A_2}{\partial t} = (a-1)A_2 - \frac{A_2}{\dot{\gamma}_2^2}\{3|A_2|^2 + 2|A_1|^2[2+\cos(4\varphi)]\}. \quad (6)$$

Assuming $|A_1| = |A_2| = |A_s|$, the nontrivial amplitude of the stationary solution becomes

$$|A_s| = \dot{\gamma}_2 \left[\frac{a-1}{7+2\cos(4\varphi)}\right]^{1/2}. \quad (7)$$

A linear stability analysis yields the resulting decay and/or growth rates,

$$\lambda_- = -2(a-1), \qquad \lambda_+ = \frac{2(a-1)[1+2\cos(4\varphi)]}{7+2\cos(4\varphi)}, \quad (8)$$

where only λ_+ can become positive for $a > 1$ and, thus, determines stability.

Whether the stationary solution is stable is determined by the angle φ; see Fig. 3(a). In particular, perpendicular configurations of $\varphi = \pi/2$ are unstable ($\lambda_+ > 0$), whereas configurations of $\varphi = \pi/4$ are stable ($\lambda_+ < 0$). These analytical results confirm our numerical observations and explain the geometry of the vortex lattice. Therefore, shear thickening leads to skewed lattices of $\varphi \neq \pi/2$ and vortex elongation along a common axis $\mathbf{n}$. In Fig. 1(a), $\mathbf{n}$ is
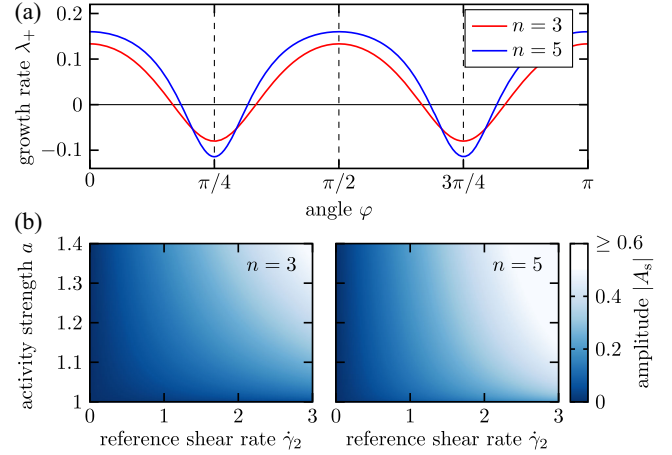

FIG. 3. Results obtained from the amplitude equations. (a) Maximum growth rate of perturbations with respect to the stationary solution for $n = 3$ [Eq. (8)] and $n = 5$ [67] as a function of the angle φ between the two modes representing the vortex pattern. (b) Amplitude $|A_s|$ of the stationary solution at $\varphi = \pi/4$ as a function of a and $\dot{\gamma}_2$ for $n = 3$ [Eq. (7)] and for $n = 5$ [67].

inclined by an angle of $3\pi/8$ from each wave vector. The case of $n = 5$ [67] leads to similar results, yet with a slightly narrower region of stability; see Fig. 3(a).

Because of the nonlinear nature of advection, destabilization becomes more important with increasing amplitude of the emerging patterns. To explore this point, we plot the stationary amplitude according to Eq. (7) for $n = 3$ and for $n = 5$ [67] in Fig. 3(b). It grows with increasing activity a and reference shear rate $\dot{\gamma}_2$. This is caused by pattern saturation being mediated via shear-thickening effects and thus becoming stronger when these set in earlier, that is, for smaller $\dot{\gamma}_2$. Comparing Fig. 3(b) with the correlation times τ displayed in Fig. 2(a) adds to this point. Increasing a or $\dot{\gamma}_2$ leads to faster dynamics of the flow field and thus to a more turbulent state. The dependence of A_s on the reference shear rate $\dot{\gamma}_2$ is linear in Eq. (7). This implies substantial impact of variations in $\dot{\gamma}_2$ on the emerging spatiotemporal structures, in line with the results for the correlation time τ and the degree of nematic order $|q|$ shown in Fig. 2 for different values of n.

As an immediate perspective, the emerging regular vortex patterns facilitate the spatial organization of objects within the system. To demonstrate this effect, we consider the dynamics of passively advected particles of intermediate size and perform additional simulations using a simplified form of the Maxey-Riley equation [69,71] coupled to the flow field obtained via Eq. (4); see Ref. [67] for details. As is known from particle-laden flows [69–72], passive objects tend to accumulate in certain areas of the flow if their density ρ_p is different from that of the carrier fluid ρ_s. Lighter objects cluster within vortices, whereas heavier objects are ejected from them [73]. The density ratio is characterized by the factor $R = 2\rho_s/(\rho_s + 2\rho_p)$.
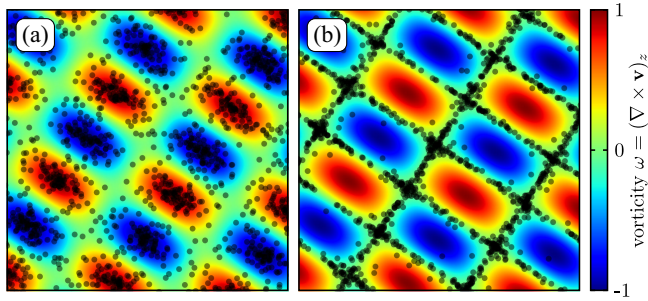
FIG. 4. Spatial organization of passive particles (dark dots) of diameter $d = 0.06\Lambda_c$ at St = 0.033 in an active shear-thickening carrier fluid at time $t = 16\,000$ after starting from random initial distributions. (a) Lighter particles (here half the fluid density, $R = 1$) cluster in vortex centers, whereas (b) heavier particles (here twice the fluid density, $R = 2/5$) accumulate between vortices. Snapshot size is $6\pi \times 6\pi$.

We further introduce the Stokes number St, which measures the characteristic timescale of the particle dynamics relative to that of the flow. Under present scaling, St is defined via St $= 8\pi^2 d^2/(9\Lambda_c^2)$, which grows quadratically with the particle diameter and vanishes for point particles [67]. These effects in combination with the self-supported regular pattern formation of our active shear-thickening carrier fluid can be used to spatially organize objects into regular periodic structures; see Fig. 4 for snapshots from the numerical simulations at St = 0.033 and different density ratios. Thus, intrinsic pattern formation in shear-thickening active suspensions opens a new strategy of generating sheets of functionalized metamaterials based on regular positional structuring of embedded objects on the microscale [6,8].

To summarize, we reveal that shear thickening is able to reorganize the flow field in active suspensions and intrinsically stabilizes regular vortex patterns in an otherwise turbulent state. Elongation arises for the vortices along a common axis. In contrast to other related observations on suspensions of active microswimmers, the patterns here are intrinsically stabilized by the shear-thickening carrier liquid and do not require external stabilization via geometrical constraints, such as arrangements of small obstacles [31–35], systems of coupled flow chambers [28–30], or substrate friction [76]. The effect can therefore be employed to intrinsically structure functionalized components on the micrometer scale. Changing the properties of the microswimmers, for instance, self-swimming speed or body size, allows us to tune the intrinsic selection of length scales [17] and thus the lattice constant of the stabilized patterns.

*henning.reinken@ovgu.de
†a.menzel@ovgu.de

[1] Y. Sawa, F. Ye, K. Urayama, T. Takigawa, V. Gimenez-Pinto, R. L. B. Selinger, and J. V. Selinger, Shape selection of twist-nematic-elastomer ribbons, Proc. Natl. Acad. Sci. U.S.A. **108**, 6364 (2011).

[2] T. H. Ware, M. E. McConney, J. J. Wie, V. P. Tondiglia, and T. J. White, Voxelated liquid crystal elastomers, Science **347**, 982 (2015).

[3] A. S. Gladman, E. A. Matsumoto, R. G. Nuzzo, L. Mahadevan, and J. A. Lewis, Biomimetic 4d printing, Nat. Mater. **15**, 413 (2016).

[4] A. Giudici, A. Clement, D. L. Duffy, M. R. Shankar, and J. S. Biggins, Multiple shapes from a single nematic elastomer sheet activated via patterned illumination, Europhys. Lett. **140**, 36003 (2022).

[5] M. I. Hussein, M. J. Leamy, and M. Ruzzene, Dynamics of phononic materials and structures: Historical origins, recent progress, and future outlook, Appl. Mech. Rev. **66**, 040802 (2014).

[6] J. Baumgartl, M. Zvyagolskaya, and C. Bechinger, Tailoring of phononic band structures in colloidal crystals, Phys. Rev. Lett. **99**, 205503 (2007).

[7] M. Caleap and B. W. Drinkwater, Acoustically trapped colloidal crystals that are reconfigurable in real time, Proc. Natl. Acad. Sci. U.S.A. **111**, 6226 (2014).

[8] M. Oudich, N. J. Gerard, Y. Deng, and Y. Jing, Tailoring structure-borne sound through bandgap engineering in phononic crystals and metamaterials: A comprehensive review, Adv. Funct. Mater. **33**, 2206309 (2023).

[9] M. C. Marchetti, J. F. Joanny, S. Ramaswamy, T. B. Liverpool, J. Prost, M. Rao, and R. A. Simha, Hydrodynamics of soft active matter, Rev. Mod. Phys. **85**, 1143 (2013).

[10] C. Bechinger, R. Di Leonardo, H. Löwen, C. Reichhardt, G. Volpe, and G. Volpe, Active particles in complex and crowded environments, Rev. Mod. Phys. **88**, 045006 (2016).

[11] A. Doostmohammadi, J. Ignés-Mullol, J. M. Yeomans, and F. Sagués, Active nematics, Nat. Commun. **9**, 3246 (2018).

[12] M. Bär, R. Großmann, S. Heidenreich, and F. Peruani, Self-propelled rods: Insights and perspectives for active matter, Annu. Rev. Condens. Matter Phys. **11**, 441 (2020).

[13] G. Gompper, R. G. Winkler, T. Speck, A. Solon, C. Nardini, F. Peruani, H. Löwen, R. Golestanian, U. B. Kaupp, L. Alvarez *et al.*, The 2020 motile active matter roadmap, J. Phys. Condens. Matter **32**, 193001 (2020).

[14] C. Dombrowski, L. Cisneros, S. Chatkaew, R. E. Goldstein, and J. O. Kessler, Self-concentration and large-scale coherence in bacterial dynamics, Phys. Rev. Lett. **93**, 098103 (2004).

[15] A. Sokolov, I. S. Aranson, J. O. Kessler, and R. E. Goldstein, Concentration dependence of the collective dynamics of swimming bacteria, Phys. Rev. Lett. **98**, 158102 (2007).

[16] L. H. Cisneros, R. Cortez, C. Dombrowski, R. E. Goldstein, and J. O. Kessler, Fluid dynamics of self-propelled microorganisms, from individuals to concentrated populations, Exp. Fluids **43**, 737 (2007).

[17] A. Sokolov and I. S. Aranson, Physical properties of collective motion in suspensions of bacteria, Phys. Rev. Lett. **109,** 248109 (2012).

[18] H. Reinken, S. H. L. Klapp, M. Bär, and S. Heidenreich, Derivation of a hydrodynamic theory for mesoscale dynamics in microswimmer suspensions, Phys. Rev. E **97,** 022613 (2018).

[19] R. Alert, J. Casademunt, and J.-F. Joanny, Active turbulence, Annu. Rev. Condens. Matter Phys. **13** (2022).

[20] A. Sokolov, M. M. Apodaca, B. A. Grzybowski, and I. S. Aranson, Swimming bacteria power microscopic gears, Proc. Natl. Acad. Sci. U.S.A. **107,** 969 (2010).

[21] A. Kaiser, A. Peshkov, A. Sokolov, B. ten Hagen, H. Löwen, and I. S. Aranson, Transport powered by bacterial turbulence, Phys. Rev. Lett. **112,** 158101 (2014).

[22] M. J. Kim and K. S. Breuer, Controlled mixing in microfluidic systems using bacterial chemotaxis, Anal. Chem. **79,** 955 (2007).

[23] Y. K. Suh and S. Kang, A review on mixing in microfluidics, Micromachines **1,** 82 (2010).

[24] R. R. Trivedi, R. Maeda, N. L. Abbott, S. E. Spagnolie, and D. B. Weibel, Bacterial transport of colloids in liquid crystalline environments, Soft Matter **11,** 8404 (2015).

[25] A. Sokolov, S. Zhou, O. D. Lavrentovich, and I. S. Aranson, Individual behavior and pairwise interactions between microswimmers in anisotropic liquid, Phys. Rev. E **91,** 013009 (2015).

[26] L. Schwarz, M. Medina-Sánchez, and O. G. Schmidt, Hybrid biomicromotors, Appl. Phys. Rev. **4,** 031301 (2017).

[27] H. Reinken, S. Heidenreich, M. Baer, and S. H. L. Klapp, Anisotropic mesoscale turbulence and pattern formation in microswimmer suspensions induced by orienting external fields, New J. Phys. **21,** 013037 (2019).

[28] H. Wioland, F. G. Woodhouse, J. Dunkel, J. O. Kessler, and R. E. Goldstein, Confinement stabilizes a bacterial suspension into a spiral vortex, Phys. Rev. Lett. **110,** 268102 (2013).

[29] E. Lushi, H. Wioland, and R. E. Goldstein, Fluid flows created by swimming bacteria drive self-organization in confined suspensions, Proc. Natl. Acad. Sci. U.S.A. **111,** 9733 (2014).

[30] H. Wioland, F. G. Woodhouse, J. Dunkel, and R. E. Goldstein, Ferromagnetic and antiferromagnetic order in bacterial vortex lattices, Nat. Phys. **12,** 341 (2016).

[31] D. Nishiguchi, I. S. Aranson, A. Snezhko, and A. Sokolov, Engineering bacterial vortex lattice via direct laser lithography, Nat. Commun. **9,** 4486 (2018).

[32] K. Sone and Y. Ashida, Anomalous topological active matter, Phys. Rev. Lett. **123,** 205502 (2019).

[33] H. Reinken, D. Nishiguchi, S. Heidenreich, A. Sokolov, M. Bär, S. H. L. Klapp, and I. S. Aranson, Organizing bacterial vortex lattices by periodic obstacle arrays, Commun. Phys. **3,** 76 (2020).

[34] B. Zhang, B. Hilton, C. Short, A. Souslov, and A. Snezhko, Oscillatory chiral flows in confined active fluids with obstacles, Phys. Rev. Res. **2,** 043225 (2020).

[35] H. Reinken, S. Heidenreich, M. Bär, and S. H. L. Klapp, Ising-like critical behavior of vortex lattices in an active fluid, Phys. Rev. Lett. **128,** 048004 (2022).

[36] J. Teran, L. Fauci, and M. Shelley, Viscoelastic fluid response can increase the speed and efficiency of a free swimmer, Phys. Rev. Lett. **104,** 038101 (2010).

[37] C. Datt, B. Nasouri, and G. J. Elfring, Two-sphere swimmers in viscoelastic fluids, Phys. Rev. Fluids **3,** 123301 (2018).

[38] M. Puljiz and A. M. Menzel, Memory-based mediated interactions between rigid particulate inclusions in viscoelastic environments, Phys. Rev. E **99,** 012601 (2019).

[39] K. Yasuda, M. Kuroda, and S. Komura, Reciprocal microswimmers in a viscoelastic fluid, Phys. Fluids **32,** 093102 (2020).

[40] G. Li, E. Lauga, and A. M. Ardekani, Microswimming in viscoelastic fluids, J. Nonnewton. Fluid Mech. **297,** 104655 (2021).

[41] M. Eberhard, A. Choudhary, and H. Stark, Why the reciprocal two-sphere swimmer moves in a viscoelastic environment, Phys. Fluids **35,** 063119 (2023).

[42] T. D. Montenegro-Johnson, D. J. Smith, and D. Loghin, Physics of rheologically enhanced propulsion: Different strokes in generalized Stokes, Phys. Fluids **25,** 081903 (2013).

[43] T. Qiu, T.-C. Lee, A. G. Mark, K. I. Morozov, R. Münster, O. Mierka, S. Turek, A. M. Leshansky, and P. Fischer, Swimming by reciprocal motion at low Reynolds number, Nat. Commun. **5,** 5119 (2014).

[44] G. Li and A. M. Ardekani, Undulatory swimming in non-Newtonian fluids, J. Fluid Mech. **784,** R4 (2015).

[45] C. Datt, L. Zhu, G. J. Elfring, and O. S. Pak, Squirming through shear-thinning fluids, J. Fluid Mech. **784,** R1 (2015).

[46] A. J. T. M. Mathijssen, T. N. Shendruk, J. M. Yeomans, and A. Doostmohammadi, Upstream swimming in microbiological flows, Phys. Rev. Lett. **116,** 028104 (2016).

[47] B. van Gogh, E. Demir, D. Palaniappan, and O. S. Pak, The effect of particle geometry on squirming through a shear-thinning fluid, J. Fluid Mech. **938,** A3 (2022).

[48] Y. Bozorgi and P. T. Underhill, Effect of viscoelasticity on the collective behavior of swimming microorganisms, Phys. Rev. E **84,** 061901 (2011).

[49] Y. Bozorgi and P. T. Underhill, Role of linear viscoelasticity and rotational diffusivity on the collective behavior of active particles, J. Rheol. **57,** 511 (2013).

[50] Y. Bozorgi and P. T. Underhill, Effects of elasticity on the nonlinear collective dynamics of self-propelled particles, J. Nonnewton. Fluid Mech. **214,** 69 (2014).

[51] E. J. Hemingway, A. Maitra, S. Banerjee, M. C. Marchetti, S. Ramaswamy, S. M. Fielding, and M. E. Cates, Active viscoelastic matter: From bacterial drag reduction to turbulent solids, Phys. Rev. Lett. **114,** 098302 (2015).

[52] E. J. Hemingway, M. E. Cates, and S. M. Fielding, Viscoelastic and elastomeric active matter: Linear instability and nonlinear dynamics, Phys. Rev. E **93,** 032702 (2016).

[53] G. Li and A. M. Ardekani, Collective motion of microorganisms in a viscoelastic fluid, Phys. Rev. Lett. **117,** 118001 (2016).

[54] E. L. C. VI M. Plan, J. M. Yeomans, and A. Doostmohammadi, Active matter in a viscoelastic environment, Phys. Rev. Fluids **5,** 023102 (2020).

[55] S. Liu, S. Shankar, M. C. Marchetti, and Y. Wu, Viscoelastic control of spatiotemporal order in bacterial active matter, Nature (London) **590,** 80 (2021).

[56] J. Słomka and J. Dunkel, Generalized Navier-Stokes equations for active suspensions, Eur. Phys. J. Special Topics **224**, 1349 (2015).

[57] J. Słomka and J. Dunkel, Geometry-dependent viscosity reduction in sheared active fluids, Phys. Rev. Fluids **2**, 043102 (2017).

[58] J. Słomka and J. Dunkel, Spontaneous mirror-symmetry breaking induces inverse energy cascade in 3d active fluids, Proc. Natl. Acad. Sci. U.S.A. **114**, 2119 (2017).

[59] J. Słomka, P. Suwara, and J. Dunkel, The nature of triad interactions in active turbulence, J. Fluid Mech. **841**, 702 (2018).

[60] H. H. Wensink, J. Dunkel, S. Heidenreich, K. Drescher, R. E. Goldstein, H. Löwen, and J. M. Yeomans, Meso-scale turbulence in living fluids, Proc. Natl. Acad. Sci. U.S.A. **109**, 14308 (2012).

[61] C. W. Wolgemuth and J. I. Palos-Chavez, Continuum dynamics of suspensions at low Reynolds number, J. Fluid Mech. **966**, A16 (2023).

[62] P. A. Davidson, *Turbulence: An Introduction for Scientists and Engineers* (Oxford University Press, New York, 2015).

[63] S. Mukherjee, R. K. Singh, M. James, and S. S. Ray, Intermittency, fluctuations and maximal chaos in an emergent universal state of active turbulence, Nat. Phys. **19**, 891 (2023).

[64] A. de Waele, Viscometry and Plastometry, J. Oil Color Chem. Assoc. **6**, 33 (1923).

[65] W. Ostwald, Ueber die Geschwindigkeitsfunktion der Viskosität disperser Systeme. I, Kolloid Z. **36**, 99 (1925).

[66] F. Irgens, *Rheology and Non-Newtonian Fluids* (Springer, New York, 2014).

[67] See Supplemental Material at http://link.aps.org/supplemental/10.1103/PhysRevLett.132.138301 for details on our numerical method, additional information on how the correlation time τ and the nematic order parameter q are calculated, details on the derivation of the amplitude equations (6) for $n = 3$, the amplitude equations for $n = 5$, and more information on the transport of passive objects within the flow and its numerical implementation.

[68] J. Dunkel, S. Heidenreich, K. Drescher, H. H. Wensink, M. Bär, and R. E. Goldstein, Fluid dynamics of bacterial turbulence, Phys. Rev. Lett. **110**, 228102 (2013).

[69] M. R. Maxey and J. J. Riley, Equation of motion for a small rigid sphere in a nonuniform flow, Phys. Fluids **26**, 883 (1983).

[70] L. Brandt and F. Coletti, Particle-laden turbulence: Progress and perspectives, Annu. Rev. Fluid Mech. **54**, 159 (2022).

[71] G. Haller and T. Sapsis, Where do inertial particles go in fluid flows?, Physica (Amsterdam) **237D**, 573 (2008).

[72] S. Balachandar and J. K. Eaton, Turbulent dispersed multiphase flow, Annu. Rev. Fluid Mech. **42**, 111 (2010).

[73] J. K. Eaton and J. Fessler, Preferential concentration of particles by turbulence, Int. J. Multiphase Flow **20**, 169 (1994).

[74] M. Cross and H. Greenside, *Pattern Formation and Dynamics in Nonequilibrium Systems* (Cambridge University Press, Cambridge, 2009).

[75] A. Meurer *et al.*, SymPy: Symbolic computing in PYTHON, PeerJ Comput. Sci. **3**, e103 (2017).

[76] A. Doostmohammadi, M. F. Adamer, S. P. Thampi, and J. M. Yeomans, Stabilization of active matter by flow-vortex lattices and defect ordering, Nat. Commun. **7**, 10557 (2016).